

The study of Kr^+ ion irradiation and thermal post-annealing on structural and magnetic properties of Pt/Co bilayers

Roman Pedan¹, Ivan Kruhlov¹ , Pavlo Makushko², Oleksandr Dubikovskiy^{1,3},
Oleksandr Kosulya³ , Andrii Burmak¹, Andrii Orlov¹, Andrii Bodnaruk^{1,4},
Vladimir Golub⁵, Jürgen Fassbender², Denys Makarov^{2,*}  and Igor Vladymyrskiy^{1,*} 

¹ National Technical University of Ukraine ‘Igor Sikorsky Kyiv Polytechnic Institute’, Prospect Beresteyskiy 37, Kyiv 03056, Ukraine

² Helmholtz-Zentrum Dresden-Rossendorf e.V., Institute of Ion Beam Physics and Materials Research, Bautzner Landstrasse 400, 01328 Dresden, Germany

³ V. Lashkaryov Institute of Semiconductor Physics, National Academy of Sciences of Ukraine, Prospect Nauky 41, Kyiv 03680, Ukraine

⁴ Institute of Physics, National Academy of Sciences of Ukraine, Prospect Nauky 46, Kyiv 03028, Ukraine

⁵ V.G. Baryakhtar Institute of Magnetism, National Academy of Sciences of Ukraine, 36-B Vernadsky Blvd., Kyiv 03142, Ukraine

E-mail: d.makarov@hzdr.de and vladymyrskiy@kpm.kpi.ua

Received 21 July 2025, revised 20 October 2025

Accepted for publication 28 October 2025

Published 7 November 2025



Abstract

Co–Pt thin films gained particular interest for applications in magnetic data storage and spintronics. Here, we report on the modification of structural and magnetic properties of Pt/Co bilayer stacks after 110 keV Kr^+ irradiation with ion fluence varied from 1×10^{14} ions cm^{-2} to 1×10^{15} ions cm^{-2} followed by post-irradiation annealing at 550 °C for 30 min. Structural characterization revealed that ion irradiation alone induces layers intermixing, leading to the formation of an equiatomic and Pt-rich Co–Pt solid solutions of varied atomic concentrations depending on the applied fluence. Post-annealing changes the fraction of these phases but does not result in the formation of a single phase sample. The coexistence of two magnetic phases makes the interpretation of the magnetic properties cumbersome. We observe a decrease of the effective magnetization with fluence, which corresponds to the transformation of the elemental Co in the initial stacks into Co–Pt alloy. The effective thickness of the magnetic phase increases with ion beam and thermal processing from about the nominal thickness of the Co layer to the thickness of the entire layer stack. By comparing the results of the Kr^+ irradiation of Pt/Co bilayers with the literature data on the irradiation with lighter Ar^+ and N^+ ions, we demonstrate versatility of the ion beam techniques in tailoring the material properties of Co–Pt systems in a broad range, which can be adjusted with respect to a specific application.

* Authors to whom any correspondence should be addressed.



Original content from this work may be used under the terms of the [Creative Commons Attribution 4.0 licence](https://creativecommons.org/licenses/by/4.0/). Any further distribution of this work must maintain attribution to the author(s) and the title of the work, journal citation and DOI.

Supplementary material for this article is available [online](#)

Keywords: ion irradiation, ferromagnetic thin films, CoPt alloy, diffusion, phase formation

1. Introduction

Ion irradiation stands as one of the key materials science approaches, enabling the precise exposure of materials to energetic ion beams [1]. This technique is widely used in semiconductor technologies [2, 3], photo- and electrocatalytic applications [4], surface hardening [5–8], modification of materials physical properties [9, 10], surface etching and depth profiling in materials analysis [11, 12] to name just a few. Fundamentally, the study of ion beam treatment of different material families provides understanding of atomic-level processes [13], material transformation [14, 15], and effects of radiation-induced damage [16].

Irradiation by light and heavy projectiles is also widely applied to modify properties of magnetic materials including technologically relevant magnetic thin films [17], such as Fe–Rh [18], Ni–Fe [19], Mn–As [20], Mn–Ga [21], Mn–Al [22]. The irradiation effect on thin films is complex, involving numerous processes such as atomic displacement, ion implantation, clustering, and mixing. At elevated fluence and/or energy of ion beam, the transfer of kinetic energy from incident particles to the irradiated surface may cause changes in its chemical and phase composition, thus affecting the structural and magnetic properties of the material. For instance, Gupta *et al* have observed an increase of the lattice parameter, a pronounced improvement of crystallinity, and an enlargement in the coercivity in permalloy ($\text{Ni}_{79}\text{Fe}_{21}$) thin films after they have been irradiated by 75 keV Ar^+ and 140 keV Kr^+ ions [23]. Hasegawa *et al* have reported the structural transition from $L1_0$ to A1 phase in FePt thin films upon irradiation by 2–35 keV B^+ , Cr^+ , Ga^+ , and Nb^+ ions [24]. Notably, for heavier ions (i.e. Ga^+ , Nb^+), a fluence of 0.05 at.% (8×10^{13} ions cm^{-2}) was sufficient for $L1_0 \rightarrow \text{A1}$ structural transition, while a significantly higher fluence of 1 at.% was required for lighter ions (i.e. B^+ , Cr^+). At the same time, a substantial increase of the surface roughness has been observed for samples treated with heavier ions, whereas no appreciable changes were observed for the case of light ions. Generally, heavier ions typically produce more pronounced collision-induced intermixing and surface roughness compared to lighter ions [17].

Among different magnetic materials, the Co–Pt system is of particular interest. These materials combine excellent corrosion resistance with highly tunable magnetic properties, making them promising candidates for applications in magnetic storage and memory devices [25–35]. Furthermore, they are extensively explored in spintronics, including exchange-coupled composites [36–38], spin valves [29], terahertz (THz)

emitters [39], and spin–orbit torque devices [40]. A significant amount of research has focused on using low-to-medium energy ion irradiation to modify the magnetic properties of Co–Pt thin films. For these purposes, ions such as Ar^+ , Ga^+ , and He^+ are often utilized under various processing conditions [41–43]. The use of various types of projectiles results in different effects on the characteristics of the irradiated Co–Pt material. For instance, the irradiation of Co/Pt multilayered stacks with Ar^+ ions has been applied to change the orientation of magnetization [41] and enhance the coercivity [42, 44]. The effect of irradiation with Ga^+ and He^+ ions in a wide range of fluences (10^{11} – 10^{17} ions cm^{-2}) and energy up to 2 MeV is mainly manifested in a decrease in the coercive field due to interface intermixing [42]. Raj *et al* have recently reported that He^+ ion irradiation of Pt/Co/Pt stack can be effectively applied to achieve the balance between weaker Dzyaloshinskii–Moriya interaction, chiral damping, and sufficiently strong perpendicular magnetic anisotropy [45]. Walia *et al* [27] explored swift heavy (120 MeV Ag^{+9}) ion irradiation of Co/Pt multilayers to induce $L1_0$ ordering in CoPt alloy at a fluence of 1×10^{13} ions cm^{-2} , whereas films subjected to higher fluence of 3×10^{13} ions cm^{-2} retained the disordered cubic structure. These results indicate the necessity of a precise control over applied ion fluence for effective tailoring of the structural and magnetic properties of Co/Pt stacks.

It is notable that most of the previous studies were focused on the effect of ion irradiation on the structural and magnetic characteristics of Co/Pt layer stacks. Recently, the effect of combined influence of irradiation with thermal post-irradiation annealing started to gain attention as this approach enables higher flexibility in tailoring the material properties [46]. In particular, it has been shown that applying 110 keV pre-irradiation of the Pt(10 nm)/Co(10 nm) bilayered stacks with N^+ and Ar^+ ions prior to thermal post-annealing at 550 °C for 30 min has resulted in slowdown of the layers' diffusion intermixing compared to the single-stage annealing performed at the same conditions. This phenomenon has been associated with the presence of a moderate number of implanted projectiles that hinder the mobility of Co and Pt atoms at the annealing stage. In turn, the presence of the remaining Pt between the grains of ferromagnetic A1-CoPt phase in thin-film samples caused an increase in coercive field of up to 38%. The effect on diffusion and magnetic properties was more pronounced in the samples irradiated with Ar^+ projectiles compared to N^+ ions due to larger atomic radius and mass of Ar^+ ions. These studies stimulate further explorations of the modification of structural and magnetic properties of Pt/Co stacks irradiated with heavier ions. In particular, due

to the chemical inertness and relatively high mass, Kr^+ ions can effectively transfer energy to the lattice and may be useful for creating crystal lattice defects without inducing chemical doping [47]. This makes them particularly suitable for inducing layer intermixing [48] and defect engineering both in bulk [49] and nanoscale materials [50]. Compared to lighter ions, heavy Kr^+ can provide higher recoil energy to a smaller irradiated area, which reduces the sputtering yield. Furthermore, Kr^+ allows for the production of high dose rates in short irradiation times and is very efficient at producing dense cascades [51]. Som *et al* [52] have reported that the irradiation of Co/Pt multilayers with 100 keV Kr^+ ions induces defect clustering, ion-induced mixing across the layers' interfaces, and the formation of an ordered/disordered CoPt phase. Another study by the same group [53] explored the radiation-enhanced diffusion in Co/Pt bilayers under irradiation with 50 keV Ar^+ and 200 keV Kr^+ ions at different temperatures. The most pronounced effect of enhancement in both the coercivity and the effective magnetic anisotropy was revealed for the case of Kr^+ irradiation at 200 °C. In comparison to these results, where authors observed the co-existence of CoPt and CoPt_3 phases, their following work [44] demonstrated the possibility to form only the equiatomic CoPt phase by tuning the irradiation conditions.

Here, we investigated experimentally the effect of 110 keV Kr^+ ion pre-irradiation of Pt/Co bilayered stacks at three various fluences (1×10^{14} ions cm^{-2} , 5×10^{14} ions cm^{-2} , and 1×10^{15} ions cm^{-2}) followed by post-annealing of the thin-film samples in vacuum at 550 °C for 30 min. The effect of Kr^+ ion irradiation on structural and magnetic characteristics was revealed by comparing the samples at all stages of processing: (i) just after deposition, (ii) after ion irradiation, (iii) after single-stage annealing, and (iv) after ion irradiation followed by post-annealing. We found that the initial Kr^+ irradiation of Co/Pt bilayers induces the formation of Co–Pt solid solutions, with the atomic ratio of the components being tunable depending on the ion fluence and thermal post-annealing. These phases are found to co-exist in the samples, which makes identification of integral magnetic properties based on conventional magnetometry measurements challenging. We combined ferromagnetic resonance (FMR) analysis with the vibrating sample magnetometry (VSM) data to determine the evolution of the effective magnetization and coercive field as well as the effective thickness of the magnetic phase in the samples subjected to different ion irradiation and annealing treatments.

2. Experimental procedure

The Pt(10 nm)/Co(10 nm)/substrate bilayered stacks were prepared on $\text{SiO}_2/\text{Si}(001)$ substrates at room temperature using the magnetron sputtering technique. The deposition was accomplished by sequential RF sputtering of Co and DC sputtering of Pt from individual high-purity (99.9%) metal

targets with deposition rates of 1.5 \AA s^{-1} and 2 \AA s^{-1} , respectively. The sputtering pressure of Ar plasma upon deposition was 8×10^{-4} mbar while base pressure in the chamber was maintained at 5×10^{-4} mbar. A cross-sectional transmission electron microscopy imaging of the as-deposited stack reveals a sharp interface between deposited layers and confirms their actual thickness (10 nm) [46, 54]. The as-prepared samples were irradiated with 110 keV Kr^+ ions at Balzers MPB 202 ion implanter at three fluences of 1×10^{14} ions cm^{-2} , 5×10^{14} ions cm^{-2} , and 1×10^{15} ions cm^{-2} . Upon ion irradiation, the samples were mounted on a massive (80 cm in diameter and 12 cm in height) aluminum carousel, ensuring efficient heat dissipation and limiting the sample temperature rise not exceeding 5 °C for all applied fluences. The distribution of implanted ions through the depth of the film as a result of the ion irradiation with chosen parameters was simulated using SRIM/TRIM2010 software [55]. Various fluences were chosen aiming to achieve different concentrations of implanted ions and formation of structural defects, yet avoiding severe surface etching [56]. After irradiation, stacks were post-annealed at 550 °C for 30 min in vacuum of 10^{-6} mbar and subsequently analyzed alongside the non-irradiated samples that underwent the same single-stage annealing.

The structural analysis and phase identification of the samples after deposition and different processing stages were analyzed using the x-ray diffraction (XRD) technique at Rigaku Ultima IV diffractometer (Cu- $K\alpha$ radiation) in Bragg-Brentano θ - 2θ geometry. XRD spectra were taken in the 2θ range of 20° – 60° with a step of 0.02° per 2 s at an operating voltage of 30 kV and current of 20 mA. For a more precise phase identification, an additional measurement was performed in the 2θ range of 38° – 45° with a step of 0.01° per 4 s at operating parameters of 40 kV and 40 mA. The diffraction peaks in the obtained spectra were deconvoluted using a Gaussian function. The atomic concentrations in the Co–Pt alloy formed upon irradiation/annealing were estimated based on the Vegard's approximation law by using the crystal data for Co, Co_3Pt , CoPt, CoPt_3 , Pt phases from the Powder Diffraction File database (ICDD PDF-2 2025, cards #01-070-2057, #01-071-7410, #03-065-8970, #01-071-7411, #00-015-0806). Ion irradiation is known to induce radiation defects such as vacancies, interstitials, atomic clusters, and voids. Based on the TEM data taken on sister samples to those discussed in the present paper [46], the thin films are dense. Furthermore, we note that the estimated lattice constants as a function of the CoPt alloy composition agree well with data reported previously [57, 58] (figure S1 in the supplementary information). Hence, we do not expect that the contribution from irradiation-induced defects to the overall sample composition is major. Therefore, the reported chemical composition of the Co–Pt alloy corresponds to the equilibrium $\text{Co}_{1-x}\text{Pt}_x$ concentration. Surface morphology of the stacks after deposition and subjected to the various processing conditions was examined by atomic force microscopy (AFM) using a NanoScope IIIa Dimension 3000 scanning probe

microscope. The AFM measurements were performed in tapping mode with silicon tips having a nominal apex radius of ~ 10 nm (Bruker, TESP-V2). Secondary ion mass spectrometry (SIMS) technique at Ion ToF IV device was employed for chemical depth profiling using a beam of primary 2 keV Cs^- ions. The following parameters were used for SIMS depth profiling: beam current of ~ 130 nA and sputter area of $\sim 350 \times 350 \mu\text{m}^2$, providing the beam power of ~ 0.26 mW and corresponding to a heat flux density of ~ 0.21 W cm^{-2} . Such a low heat flux density leads only to negligible local temperature rise during the measurement, keeping the sample at nearly room temperature. The magnetic characteristics were studied at room temperature, applying VSM measurements at in-plane and out-of-plane magnetic fields up to 1 kOe. The FMR analysis was carried out at Bruker ELEXYS-E500 X-band (9.86 GHz) spectrometer equipped with an automated goniometer. The angular step (θ) was set to 1° near the film normal (low θ region) and 10° over the remaining angular range.

3. Results and discussion

3.1. Structural & chemical characterization

The left part of figure 1 shows a wide-range (2θ from 20° to 60°) XRD scans of Pt/Co stacks in their as-deposited state (a), after ion pre-irradiation with various fluences (b)–(d), single-stage annealing (e), and pre-irradiation followed by annealing (f)–(h). Short-range (2θ from 38° to 45°) deconvoluted spectra are shown in front of each wide-range scan in the right part of figure 1 (panels (i)–(p)). The diffraction pattern of the as-deposited sample is dominated by a (111) peak at 39.8° corresponding to the face-centered cubic Pt. A detailed structural characterization of the as-deposited Co–Pt samples is presented in [46]. In particular, the average grain size of Pt was found to be 9 nm, and the lattice constant was ~ 3.92 Å. It is most likely that peaks from the Co phase are not observed due to its atomic scattering factor and relatively high linear attenuation coefficient in Cu radiation [59]. The corresponding chemical depth profile of the as-deposited stack (figure 2(a)) shows a relatively sharp interface between Pt and Co layers, thus confirming the bi-layered structure of the sputtered film stack. The metal's interface region also yields a signal from the CoPt complex ion, which is associated with the interfacial roughness. It is worth noting that while the actual thickness of the two metal layers being the same (10 nm), the Pt signal at the depth profile is narrower (e.g. its total sputtering duration is less) compared to Co, which is due to the difference in metals' sputtering yields [60]. A signal at the atomic mass close to Si, which is observed at the outer surface, does not belong to the substrate but is rather a measurement artefact related to the presence of surface contaminants with an atomic mass similar to the Si species [46].

After ion irradiation of Pt/Co bilayer (without annealing), the shift of Pt(111) diffraction peak towards higher 2θ angles

(figures 1(b)–(d) and (j)–(l)) indicates a progressive intermixing of the Co and Pt components and the alloying process resulting in the formation of $\text{Co}_{10}\text{Pt}_{90}$, $\text{Co}_{16}\text{Pt}_{84}$, and $\text{Co}_{25}\text{Pt}_{75}$ phases. The right shoulder of this peak in the spectra of each irradiated sample corresponds to the formation of a low amount of $\text{Co}_{50}\text{Pt}_{50}$ equiatomic phase. At the same time, the presence of a low-intensity (111) peak from Pt is still detectable in the diffraction patterns of all the irradiated stacks. The observed formation of Co-containing phases indicates that the diffusion intermixing between metals is taking place under Kr^+ irradiation, and the increase of the irradiation fluence induces more intense intermixing. This fits well with the SIMS chemical depth profiling data, where Co diffusion into the Pt layer is clearly seen for all irradiated samples (figure 2(c)–(g)). A metals intermixing is also evidenced in the broadening of the signal from the complex CoPt ion for the irradiated films (figures 2(c)–(g)). The appearance of CoPt^+ signal in the ToF-SIMS data is caused by the formation of cluster ions during the sputtering and ionization processes. While the CoPt^+ signal cannot be considered as a reliable quantitative measure of the local Co/Pt ratio, its appearance in the SIMS spectra indicates the regions with interacted Co and Pt. Again, the higher the ion fluence, the wider the CoPt complex ion signal is, indicating a more intense metals' interdiffusion. It can also be seen that with the increase in the ion fluence, the total sputtering time of the stack became shorter, which is attributed either to a difference in the sputtering rates of the initial pure metals and the formed Co–Pt alloy phase or to the difference in the defect formation. For the later, a higher fluence yields more atomic cascades and structural defects, which weaken interatomic bonds and thus simplify the atoms to be sputtered upon SIMS depth profiling.

The XRD scan of the single-stage annealed sample (figures 1(e)–(m)) reveals the coexistence of two Co Pt phases, $\text{Co}_{54}\text{Pt}_{46}$ and $\text{Co}_{50}\text{Pt}_{50}$, which exhibit comparable diffraction peak intensities and nearly equiatomic compositions. These phases are most likely laterally separated, with slight differences in chemical composition arising from local variations in the Co/Pt thickness ratio. This interpretation is consistent with the SIMS data: the corresponding depth profile (figure 2(b)) demonstrates a complete homogenization of the elemental composition, indicating that the Co Pt phases detected by XRD are uniformly distributed throughout the entire film volume. The SIMS depth profiling data also show that the total sputtering duration of the annealed-only sample (figure 2(b)) is shorter than that of the as-deposited bilayer stack (figure 2(a)), which is most likely due to the difference in the sputtering rates of the initial pure metals and the formed Co–Pt alloy phase combined with the volumetric contraction of the film resulting from the relaxation of internal stresses and the annihilation of structural defects. This densification process results from atomic rearrangements that reduce free volume and minimize the film's overall energy state.

After irradiation followed by annealing, the phase composition is more uneven. The XRD patterns from all pre-irradiated and post-annealed samples (figures 1(f)–(h) and (n)–(p)) show

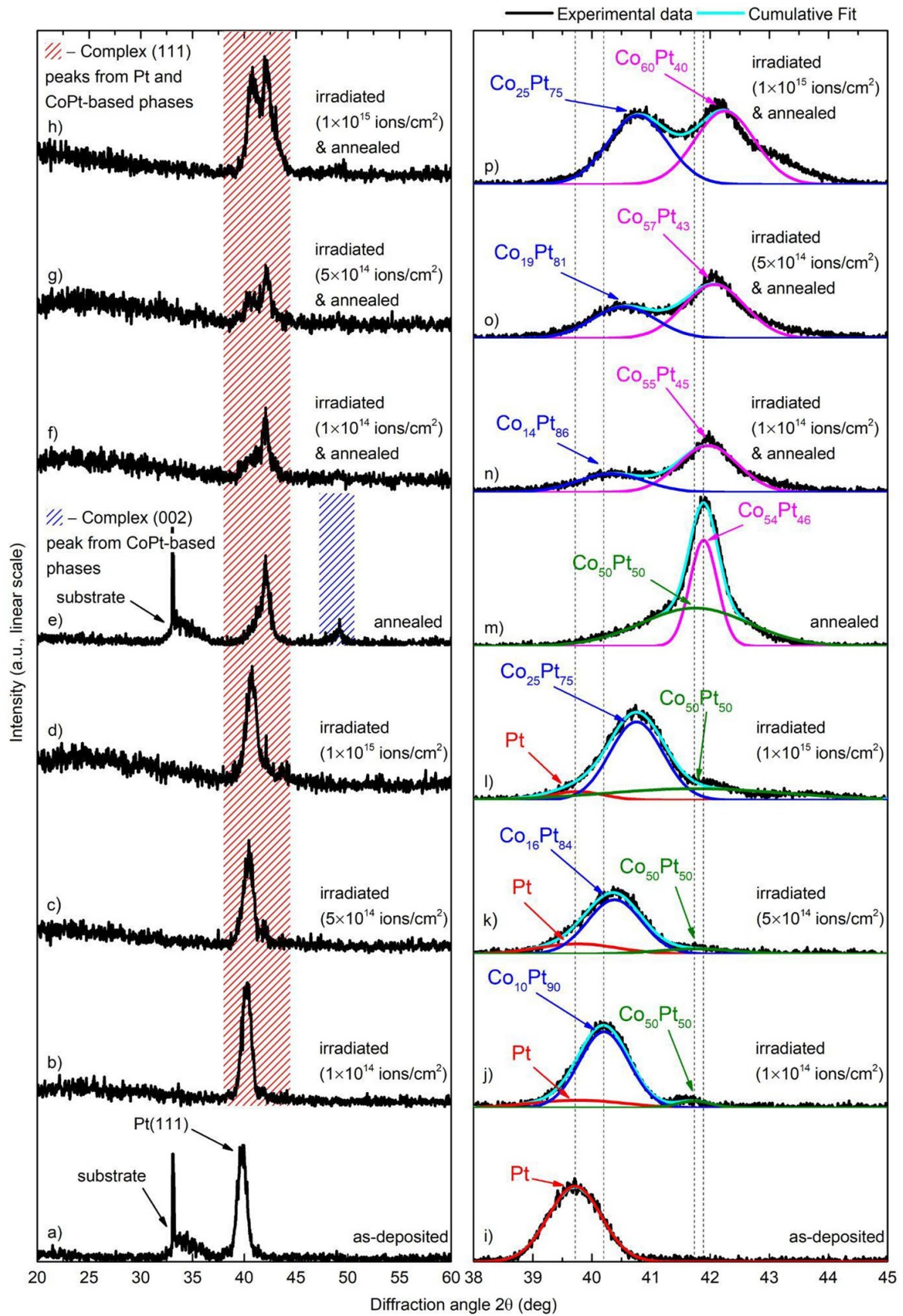


Figure 1. XRD patterns of the Pt(10 nm)/Co(10 nm)/sub. Stacks after deposition (a), (i), pre-irradiation (b)–(d), (j)–(l), single-stage annealing (e), (m), and pre-irradiation followed by post-annealing (f)–(h), (n)–(p).

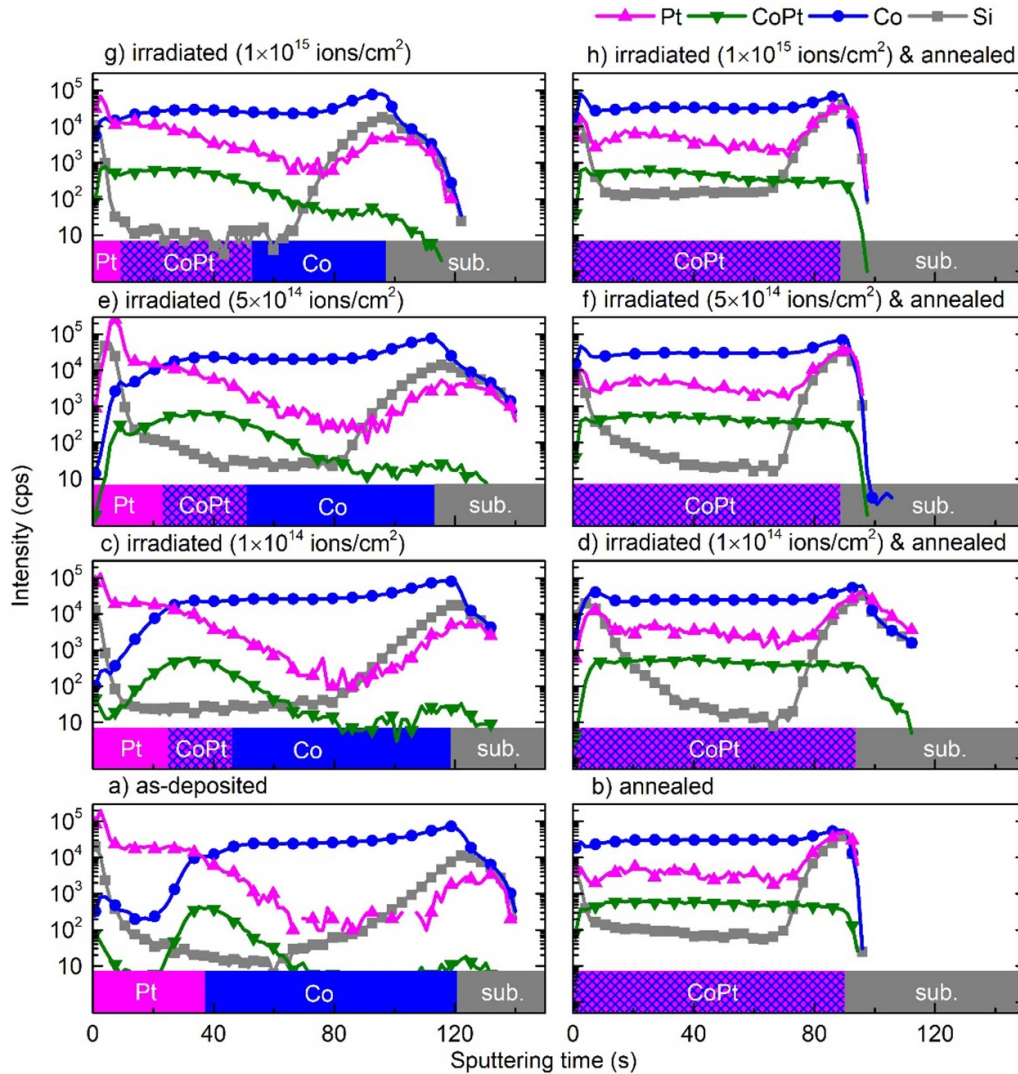


Figure 2. SIMS chemical depth profiles of the Pt(10 nm)/Co(10 nm)/sub. stack after deposition (a), pre-irradiation (c), (e), (g), single-stage annealing (b), and pre-irradiation followed by post-annealing (d), (f), (h).

the presence of Pt-rich alloys with the Co content rising from 14% for the lowest fluence to 25% for the highest fluence. Furthermore, besides a Pt-rich alloy, the diffraction peak of the near-equiatomic phase is detected. It shifts towards higher angles for higher fluences, indicating an increase of the Co content in this phase: 55% for the lowest fluence and 60% for the highest one. SIMS chemical depth profiles of the pre-irradiated and post-annealed samples (figures 1(d), (f) and (h)) demonstrate less homogeneous Pt distribution through the stack thickness compared to the single-stage annealing (figure 2(b)).

Despite a pronounced diffusion-driven intermixing, the surface morphology of the samples after post-deposition irradiation and thermal processing remains largely unchanged (figures S2–S4 in the supplementary information). AFM measurements show that the as-deposited stack exhibits a smooth

surface morphology with an RMS roughness of 0.15 nm. Post-deposition ion and/or thermal treatments result only in a slight increase of the surface roughness, with RMS values ranging from 0.45 nm to 0.65 nm, depending on the specific processing conditions. This morphological stability of ion- and/or thermally-modified material can be desirable for applications in magnetic and spintronic technologies.

Both XRD and SIMS data indicate that the diffusion intermixing between the Pt and Co layers is affected by the ion implantation and directly depends on its fluence. It follows from the SRIM/TRIM simulation data (figure 3) that the expected Kr concentrations in both metal layers are an order of magnitude higher at the highest fluence (peak concentrations are 1.6×10^{20} at cm^{-3} and 2.5×10^{20} at cm^{-3} in Pt and Co layers, respectively) than for the lowest one (corresponding peak concentrations are 2.0×10^{19} at cm^{-3} and

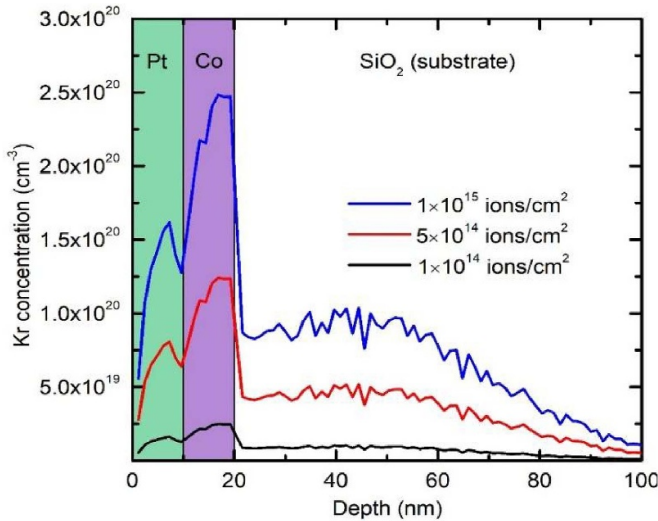


Figure 3. SRIM/TRIM simulation of the concentration of implanted Kr^+ ions as a function of the depth into the Pt(10 nm)/Co(10 nm)/sub. stack for three fluences.

2.5×10^{19} at cm^{-3}). It is worth noting that the performed simulations suggest that most of the Kr^+ projectiles stop within the metal layers rather than penetrating into the substrate, as it was observed for the samples irradiated with lighter N^+ and Ar^+ ions [46]. This behavior is attributed to a larger atomic radius and mass of Kr.

The analysis of the XRD, SIMS, and SRIM data suggests that the effect of Kr^+ irradiation on the diffusion intermixing is dual in nature and temperature dependent. The irradiation alone promotes an interdiffusion between metal layers, with a stronger intermixing at higher fluences. At this stage, the transfer of kinetic energy from Kr^+ projectiles to metal atoms plays a decisive role. However, upon subsequent post-annealing, the atomic composition of the Pt-rich phases (figure 1(j)–(i)), which have already formed during irradiation, remains nearly unchanged (figures 1(n)–(p)). Moreover, the atomic composition of the initially equiatomic phase shifts toward a higher Co content (figures 1(n)–(p)). These observations indicate that implanted Kr atoms may suppress a further composition homogenization during the following annealing process. The observed modification of the phase composition of the as-prepared Pt/Co bilayer stacks after pre-irradiation and post-annealing is visualized in the schematics shown in figure 4.

3.2. Magnetic characterization

Figure 5 demonstrates the FMR data in terms of the resonance field as a function of polar angle. The continuous red line (figure 5) is the fit to the measured resonance fields obtained from the solution of the Landau–Lifshitz equation for different polar angles. The measurements are done of

the samples after deposition, pre-irradiation at different fluences of as-prepared bilayers, post-deposition annealing, and pre-irradiation followed by post-annealing. Figure 6 shows VSM M – H magnetic hysteresis loops of all the stacks under study. These hysteresis loops in all cases are characterized by a pronounced in-plane magnetic anisotropy. The comparative representation of the FMR and VSM data is summarized in figures 7 and 8, demonstrating the dependencies of the resonance linewidth, coercivity, effective magnetization, and areal moment density as a function of the samples' treatment regimes.

The in-plane coercivity extracted from the VSM data increases after ion pre-irradiation, rising from 9 Oe in the as-deposited state to 122 Oe at the highest fluence (figure 7(c)). In the heat-treated samples, the highest coercivity of 308 Oe is observed following a single-stage annealing (figure 7(d)). For the pre-irradiated and subsequently annealed samples, the coercivity ranges from 188 Oe to 204 Oe, depending on the fluence. The resonance linewidth measured by FMR exhibits a similar trend, increasing significantly with the fluence and reaching 580 Oe for the highest fluence (figure 7(a)). In the annealed samples, the linewidth initially decreases for the samples irradiated at fluences of 1×10^{14} ions cm^{-2} and 5×10^{14} ions cm^{-2} , but then increases sharply to 1280 Oe at the highest fluence (figure 7(b)). The correspondence of these parameters indicates an increase in the anisotropy field in the pre-irradiated as well as pre-irradiated and subsequently annealed samples with increasing the irradiation fluence. The rise in the anisotropy field leads to a broadening of the resonance lines and is also related to the coercivity enhancement through the equation derived from the Stoner–Wohlfarth model for coherent magnetization rotation [61]: $H_c = 0.32 H_a$. It is also worth noting that the FMR linewidth depends not only on the magnetic anisotropy. The presence of inclusions with varying saturation magnetization leads to a linewidth broadening. Additionally, the broadening increases in the presence of non-magnetic inclusions (defects induced by irradiation and Co–Pt phases with low concentration of Co, which are nonmagnetic) due to local stray fields formed around such inclusions [62].

The effective magnetization (i.e. magnetic moment per sample's volume) derived from the FMR spectra (figure 5) is found to decrease with increasing the ion fluence—from 1210 emu cm^{-3} in the as-deposited state to 800 emu cm^{-3} at the highest fluence (figure 8(a)). A similar decline is observed for the samples subjected to thermal annealing, where the effective magnetization decreases from 960 emu cm^{-3} to 695 emu cm^{-3} (figure 8(b)). It is important to note that FMR collects the information from magnetic phases only. Without intermixing of the layers, the effective magnetization determined from FMR corresponds mainly to the magnetization of the pure Co layer. A mixing of Co and Pt with the formation of a CoPt phase, having a lower saturation magnetization in comparison with pure Co, lowers the effective magnetization

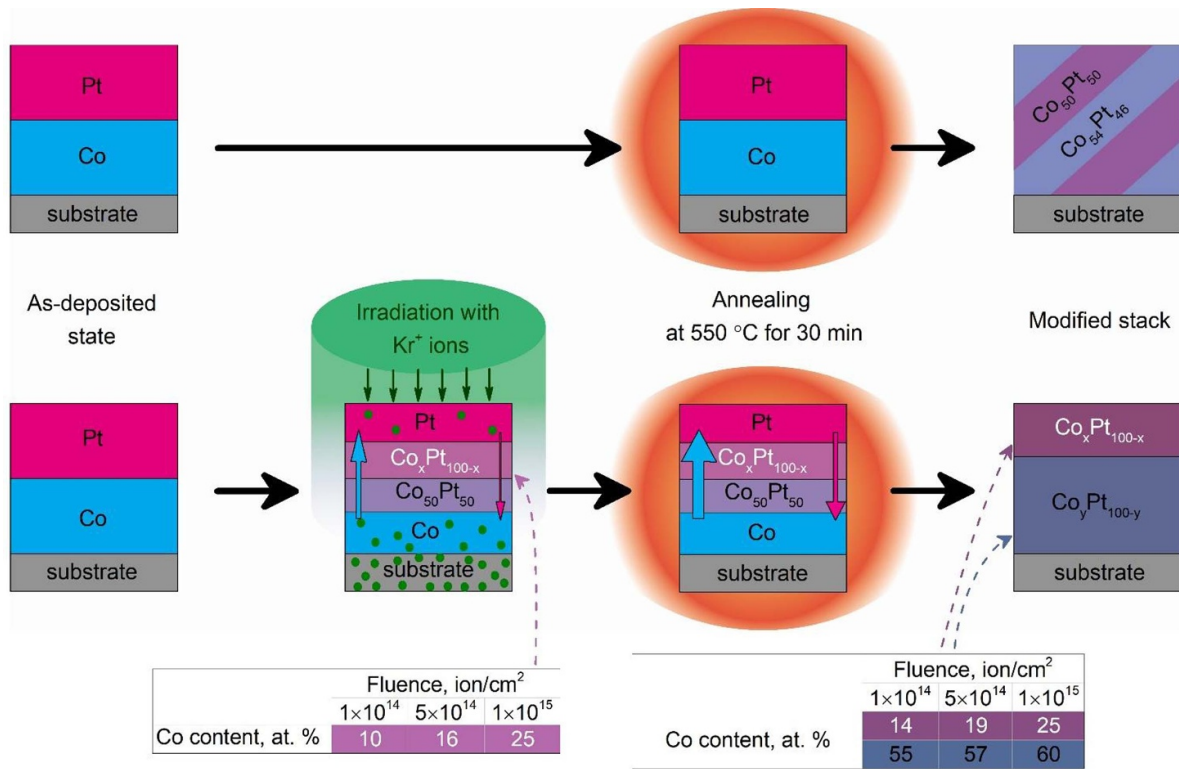


Figure 4. Schematic illustration of the irradiation- and thermally-induced modifications in chemical and phase composition of the Pt(10 nm)/Co(10 nm)/sub. Stacks.

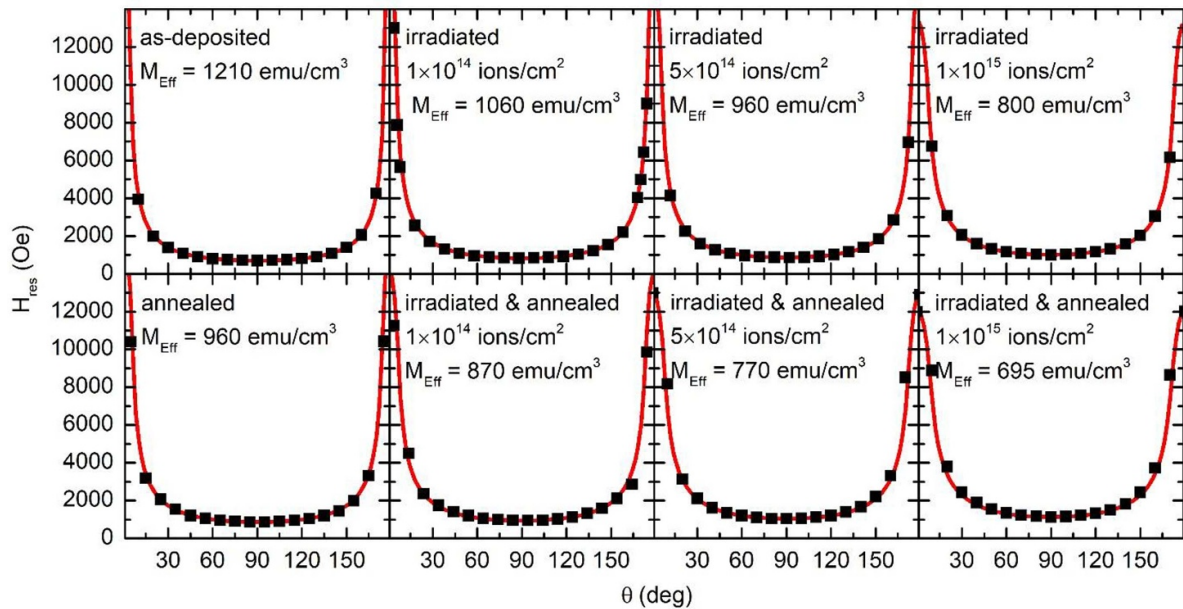


Figure 5. Resonance field as a function of the polar angle θ for the Pt(10 nm)/Co(10 nm)/sub. Stacks after deposition, pre-irradiation, single-stage annealing, and pre-irradiation followed by post-annealing.

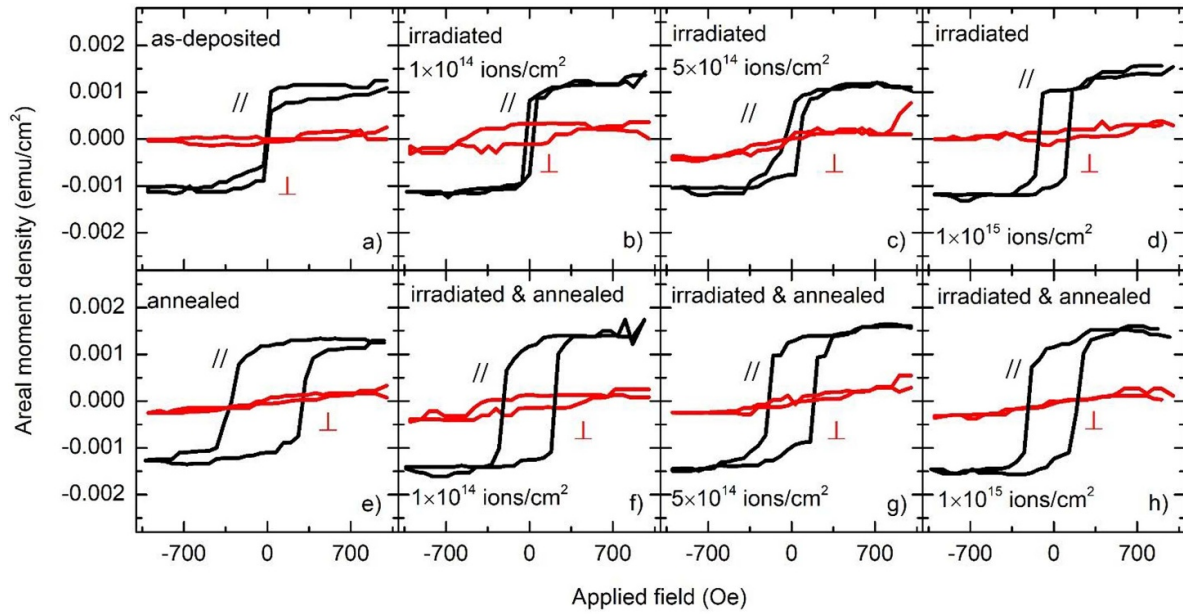


Figure 6. $M-H$ hysteresis loops of the Pt(10 nm)/Co(10 nm)/sub. Stacks after deposition (a), pre-irradiation (b)–(d), single-stage annealing (e), and pre-irradiation followed by post-annealing (f)–(h).

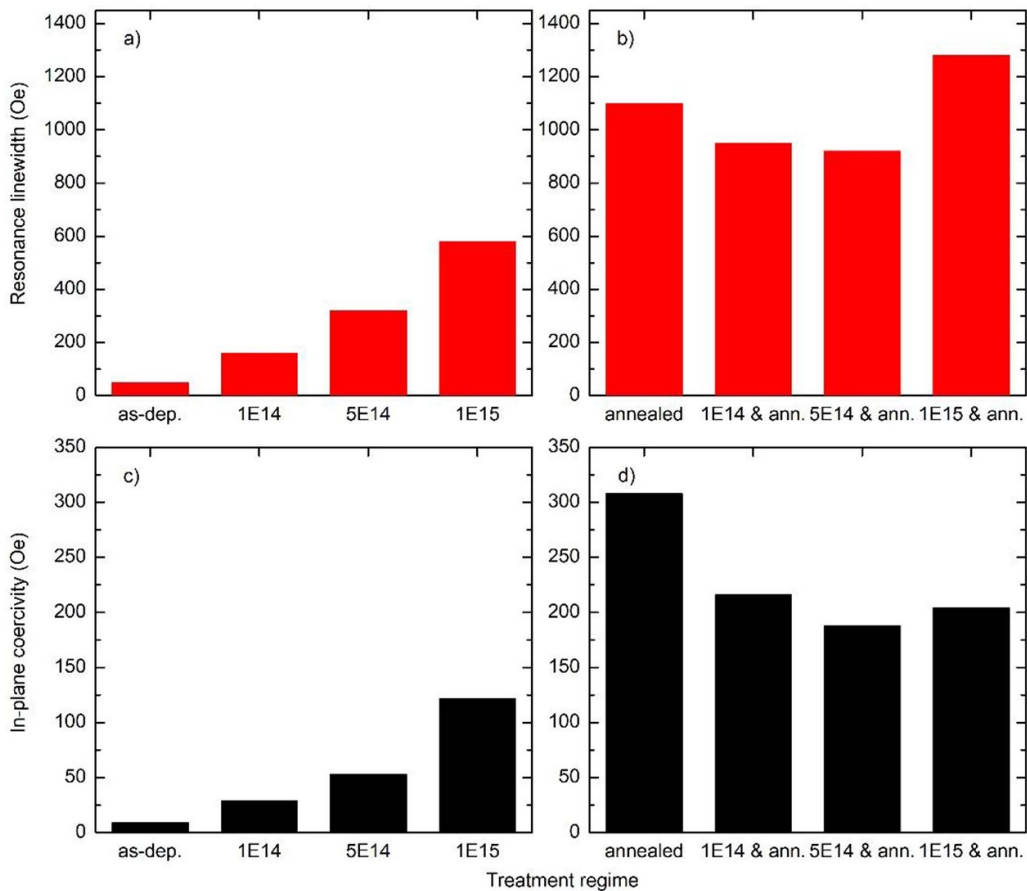


Figure 7. Resonance linewidth measured by FMR (a) and (b) and in-plane coercivity measured by VSM (c) and (d) of the Pt(10 nm)/Co(10 nm)/sub. Stacks as a function of their treatment conditions.

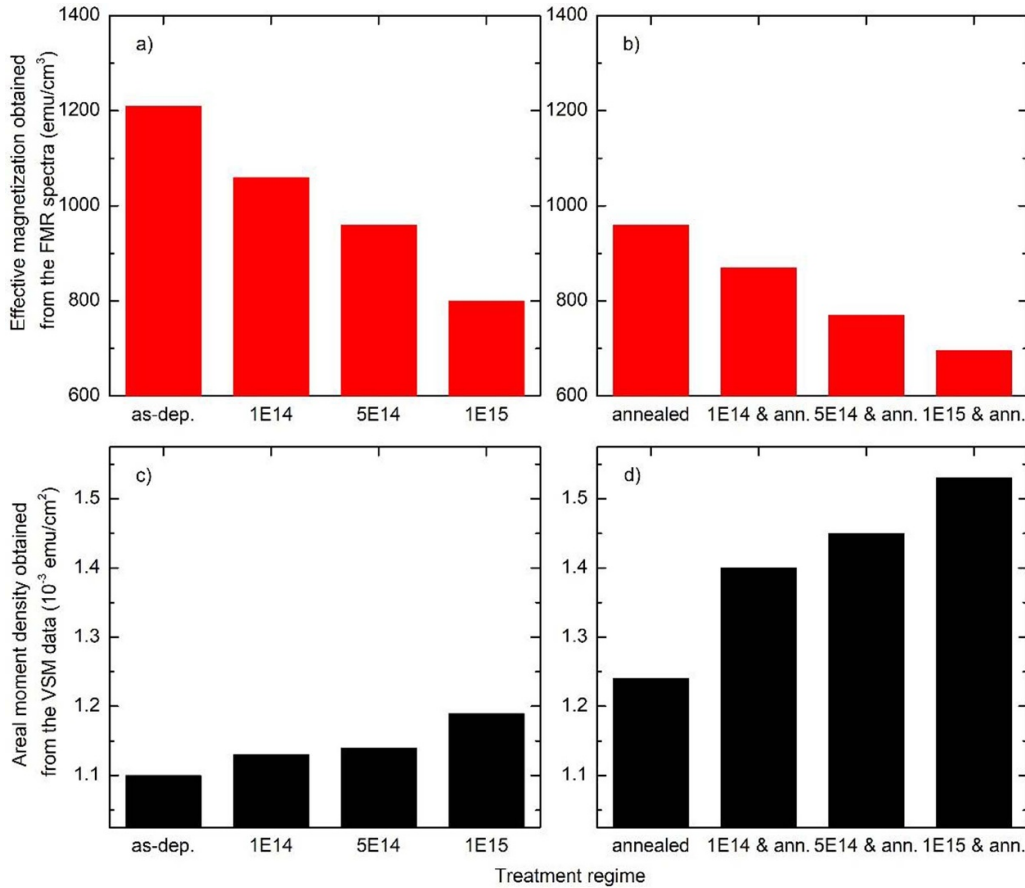


Figure 8. The effective magnetization extracted from the FMR data (a) and (b) and the areal moment density extracted from the VSM data (c), (d) of the Pt(10 nm)/Co(10 nm)/sub. Stacks as a function of their treatment conditions.

measured in FMR experiments. Besides, the presence of non-magnetic inclusions in the formed CoPt phase could lead to a decrease in the demagnetizing factor perpendicular to the film plane [63], which can also decrease the effective magnetization. The presence of the (111) texture in a nanocrystalline film indicates that the in-plane part of the cubic anisotropy is averaging out and only an out-of-plane component remains finite and can add to the perpendicular anisotropy. Based on our analysis, the corresponding anisotropy field is at most 1 kOe, which is less than 10% of the shape anisotropy field. When determining the saturation magnetization based on the FMR data, we neglect these effects, which could result in a slight underestimation of the saturation magnetization.

Since the FMR allows detecting signals from the ferromagnetic phase only, it can be inferred that, although the Co concentration in Pt-rich Co–Pt phases increases with rising irradiation fluence, the primary factor driving the change in the magnetic properties of the pre-irradiated stacks is the enhanced formation of the A1-CoPt ($\text{Co}_{50}\text{Pt}_{50}$) phase. This phase emerges due to a more intense Co–Pt intermixing, which is directly induced by the Kr^+ ion fluence. The absence of the FMR signals from the Pt-rich Co–Pt phases is likely attributed to their Curie temperatures being below room temperature, rendering them paramagnetic under the measurement

conditions [64]. In the case of the single-stage annealed stack (without pre-irradiation), the XRD analysis (figures 1(e)–(m)) reveals the coexistence of $\text{Co}_{50}\text{Pt}_{50}$ and $\text{Co}_{54}\text{Pt}_{46}$ phases. As a result of a modest 4% difference in the Co content, these phases exhibit similar magnetic properties. When irradiation is applied before annealing, Pt-rich phases are retained in the stacks. Given that the equiatomic A1-CoPt phase possesses larger coercivity compared to pure Co [65], all treated samples reveal larger in-plane coercive field compared to the as-deposited bilayer. Similarly, the samples subjected to the pre-irradiation and annealing show smaller coercivity and narrower resonance linewidth compared to the single-stage annealed stack (figures 7(b)–(d)).

Due to a complex distribution of magnetic phases within the thin films and the unknown thickness of the formed magnetic phases after various treatment modes, a direct estimation of the magnetization from the VSM measurements is challenging. Therefore, for the VSM data we provide analysis of the areal moment density, which is calculated by dividing the total magnetic moment measured by VSM by the sample area (figures 8(c) and (d)). For the as-deposited stack, the areal moment density extracted from the VSM data is 1.1×10^{-3} emu cm^{-2} (figure 8(c)). This value is attributed mainly to the ferromagnetic Co phase as well as to a possible contribution

Table 1. Saturation magnetization and coercivity of the Co–Pt alloy as a function of its elemental composition. For reference, the saturation magnetization of Co is 1420 emu cm^{-3} .

Composition	M_s , emu cm^{-3}	H_c , Oe
Co/Pt as-dep.	≈ 380 [65]	< 10 [65]
Co ₁₀ Pt ₉₀	< 100 [66] ≈ 70 [66]	100 [67, 68]
Co ₁₆ Pt ₈₄	< 200 [66, 69] ≈ 200 [70]	≈ 100 [68]
Co ₂₅ Pt ₇₅	≈ 300 [66, 69] ≈ 350 [70]	550 [67] 800 [68]
Co ₅₀ Pt ₅₀	$\approx 600\text{--}650$ [65] ≈ 668 [71] 700 [70]	300–400 [65] 350–470 [72]
Co ₅₄ Pt ₄₆	$\approx 600\text{--}800$ [66, 69] 500 [73] ≈ 715 [70]	≈ 1700 [68]
Co ₅₅ Pt ₄₅	$\approx 650\text{--}850$ [66, 69] 525 [73] ≈ 730 [70]	≈ 1700 [68]
Co ₅₇ Pt ₄₃	$\approx 700\text{--}850$ [66, 69] 560 [73] 750 [70]	≈ 1700 [68]
Co ₆₀ Pt ₄₀	≈ 750 [69] 800 [70]	≈ 1600 [68] ≈ 1000 [74]

of Pt which could be polarized due to the proximity with Co. Upon irradiation, significant intermixing between the metal layers occurs, leading to the formation of a Pt-rich Co–Pt alloy and a moderate fraction of the A1-type Co₅₀Pt₅₀ phase. The areal moment density of the irradiated samples shows a slight increase, reaching $1.2 \times 10^{-3} \text{ emu cm}^{-2}$ at the maximum fluence of $1 \times 10^{14} \text{ ions cm}^{-2}$ (figure 8(c)). A more pronounced enhancement is observed after subsequent annealing, with the areal moment density increasing to $1.53 \times 10^{-3} \text{ emu cm}^{-2}$ for the samples processed at the highest fluence (figure 8(d)).

The observed changes in the magnetization and coercivity of Co/Pt stacks subjected to various ion and/or thermal processing are associated with the difference in their elemental and phase composition. Generally, these experimental data are consistent with the literature data on magnetic properties of the Co–Pt alloy with varied composition, which are summarized in table 1. However, certain discrepancies between the magnetic data obtained in this work and literature values can be attributed to the microstructural evolution of CoPt alloyed films, which was not considered in the present analysis.

By combining the data shown in figure 8, we can get an estimate of the effective thickness of the magnetic layers, which can be calculated by dividing the areal moment density obtained from the VSM measurements by the effective magnetization derived from the FMR data. The dependence of this effective thickness on the treatment conditions is presented in

figure 9. For the as-deposited sample, the effective thickness of the magnetic phase was found to be 9.1 nm, which corresponds to the nominal thickness of the initial ferromagnetic Co layer (10 nm). Upon irradiation (without post-annealing), the effective thickness of the magnetic layer increased to 14.9 nm at the highest fluence, which is caused by larger thickness of the formed ferromagnetic Co–Pt phase compared to the thickness of the initially deposited single Co layer. For the samples subjected to pre-irradiation followed by post-annealing, the effective magnetic layer thickness exhibited clear fluence dependence: 16.1 nm for the lowest and 22.0 nm for the highest fluence. This increase indirectly reflects the volume fraction of the Co–Pt phase that contributes to the magnetic signal at room temperature.

We note a distinct difference between the effect of irradiation with heavier Kr⁺ compared to lighter N⁺ and Ar⁺ ions at a comparable fluence of $1 \times 10^{15} \text{ ions cm}^{-2}$ [46]. While any of the studied ions produces a similar effect on the metals' interdiffusion (namely, enhanced intermixing within the initial bilayered stack while hindering further composition homogenization upon subsequent post-annealing stage), a different outcome is observed in the magnetic properties. This difference is most pronounced in the samples subjected to pre-irradiation followed by post-annealing: the application of lighter N⁺ and Ar⁺ ions led to an increase in coercivity compared to the single-stage annealing, whereas irradiation with

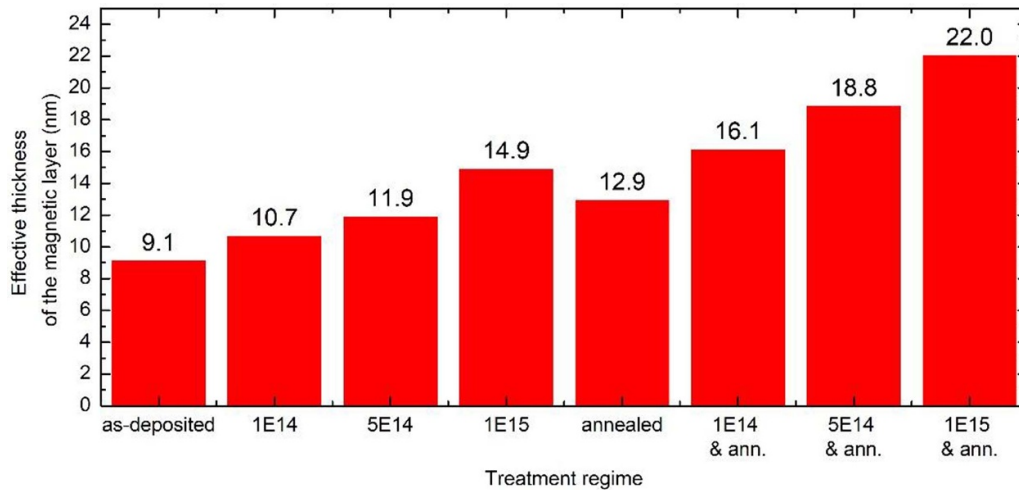


Figure 9. Effective thickness of the magnetic layer of the Pt(10 nm)/Co(10 nm)/sub. stacks as a function of their treatment conditions.

heavier Kr^+ ions resulted in reduced coercivity. This difference may be interpreted in terms of the distinct defect structures and ion implantation profiles they produce: heavy Kr^+ ions create dense, localized defect clusters and implant a high concentration of Kr atoms within the metal layers, which stabilize the partially intermixed phases during annealing by suppressing further atomic diffusion and defect migration. This structural stabilization can reduce the domain wall pinning, leading to decreased coercivity and increased saturation magnetization due to the preservation and enrichment of Co-rich ferromagnetic phases. In contrast, lighter ions produce more dispersed defects and allow for strengthening atomic diffusion and disorder upon annealing, increasing coercivity and decreasing the effective magnetization. These results demonstrate that the key magnetic properties of Co/Pt bilayers—specifically, coercivity and magnetization—can be precisely and controllably tailored over a broad range by selecting suitable ion species for irradiation combined with post-annealing.

4. Conclusions

Here, we experimentally examined the effect of 110 keV Kr^+ ion pre-irradiation of Pt(10 nm)/Co(10 nm) bilayered stacks at three various fluences (1×10^{14} ions cm^{-2} , 5×10^{14} ions cm^{-2} , and 1×10^{15} ions cm^{-2}) followed by post-annealing of the thin-film samples in vacuum at 550 °C for 30 min. We analyze the change of structural and magnetic properties of the samples at each of the processing steps. We found that the initial Kr^+ irradiation of Co/Pt bilayers induces the formation of Co–Pt solid solutions with the atomic ratio of the components being tunable depending on the ion fluence and thermal post-annealing. In particular, irradiation results in the formation of a small fraction of an equiatomic CoPt alloy and a dominant fraction of a Pt-rich Co–Pt alloy. The composition of this Pt-rich alloy increases from $\text{Co}_{10}\text{Pt}_{90}$ to $\text{Co}_{25}\text{Pt}_{75}$ with the increase of the fluence from 1×10^{14} ions cm^{-2} to 1×10^{15} ions cm^{-2} . The following

thermal post-annealing has a moderate effect on the alloy compositions and surface morphology. Still, annealing promotes the fraction of the equiatomic CoPt alloy within the sample. As these phases co-exist, it was challenging to pinpoint magnetic properties of the samples phase-specifically. The FMR characterization indicated that effective magnetization of the samples decreases with fluence, which agrees well with the transformation of a 10-nm-thick Co in the initial bilayers into a homogenized Co–Pt alloy. By combining FMR data (i.e. effective magnetization) with the VSM data (areal moment density), we were able to get access to the effective thickness of the magnetic alloy film. This effective thickness changes from about 9 nm for the as prepared samples (roughly corresponds to the nominal thickness of the Co layer) to 22 nm (roughly correspond to the total thickness of the entire stack). The obtained results on Kr^+ irradiated samples were compared to the literature data on irradiation of Pt/Co bilayers using lighter ions (Ar^+ , N^+), demonstrating that the structural and magnetic properties of Pt/Co bilayers can be tuned over a broad range in a controlled manner by appropriate choice of ion species for irradiation combined with post-annealing.

Data availability statement

The data cannot be made publicly available upon publication because they are not available in a format that is sufficiently accessible or reusable by other researchers. The data that support the findings of this study are available upon reasonable request from the authors.

Acknowledgment

The work was supported in part via the Ministry of Education and Science of Ukraine (Projects 0123U101257 and 0124U001266), the German Research Foundation (grants #MA5144/33–1, #VE 267/9–1, #VE 948/5–1), European Union in the frame of the project REGO (grant agreement

#101070066), and ERC project 3DmultiFerro (grant agreement #101141331).

Author contributions

Roman Pedan

Conceptualization (equal), Formal analysis (equal), Investigation (equal), Methodology (equal), Visualization (equal), Writing – original draft (equal), Writing – review & editing (equal)

Ivan Kruhlov  0000-0003-2078-4159

Investigation (equal), Methodology (equal), Visualization (equal), Writing – original draft (equal), Writing – review & editing (equal)

Pavlo Makushko

Investigation (equal), Methodology (equal), Writing – review & editing (equal)

Oleksandr Dubikovskiy

Investigation (equal), Methodology (equal), Visualization (equal), Writing – original draft (equal), Writing – review & editing (equal)

Oleksandr Kosulya  0000-0001-7642-8052

Investigation (equal), Methodology (equal), Visualization (equal), Writing – original draft (equal), Writing – review & editing (equal)

Andrii Burmak

Investigation (equal), Methodology (equal), Visualization (equal), Writing – original draft (equal), Writing – review & editing (equal)

Andrii Orlov

Investigation (equal), Methodology (equal), Visualization (equal), Writing – original draft (equal), Writing – review & editing (equal)

Vladimir Golub

Conceptualization (equal), Funding acquisition (equal), Investigation (equal), Methodology (equal), Project administration (equal), Supervision (equal), Visualization (equal), Writing – original draft (equal), Writing – review & editing (equal)

Jürgen Fassbender

Conceptualization (equal), Funding acquisition (equal), Methodology (equal), Supervision (equal), Writing – review & editing (equal)

Denys Makarov  0000-0002-7177-4308

Conceptualization (equal), Funding acquisition (equal), Investigation (equal), Methodology (equal), Project administration (equal), Supervision (equal), Visualization (equal), Writing – original draft (equal), Writing – review & editing (equal)

Igor Vladymyrskiy  0000-0002-2106-9176

Conceptualization (equal), Data curation (equal), Formal analysis (equal), Funding acquisition (equal),

Investigation (equal), Methodology (equal), Project administration (equal), Resources (equal), Supervision (equal), Visualization (equal), Writing – original draft (equal), Writing – review & editing (equal)

References

- [1] Huang L, Wu H, Cai G, Wu S, Li D, Jiang T, Qiao B, Jiang C and Ren F 2024 Recent progress in the application of ion beam technology in the modification and fabrication of nanostructured energy materials *ACS Nano* **18** 2578–610
- [2] Yang Z, Abas A and Cao Y 2025 Research of ultra-low concentration ion implantation on chip substrates using film delamination method combined with semiconductor simulation technology *Innov. Emerg. Technol.* **12** 2550001
- [3] Atheek P, Puviarasu P and Basha S M 2024 Impact of swift heavy ion irradiation on as-grown gallium nitride epilayers by MOCVD technique *Radiat. Phys. Chem.* **216** 111430
- [4] Huang S, Yue C, Uvdal K and Hu Z 2024 Recent advances in irradiation-mediated synthesis and tailoring of inorganic nanomaterials for photo-/electrocatalysis *Nanoscale Adv.* **7** 384–418
- [5] Jeong H-Y, Lee S, Lee S, Chang D-S, Lee J G and Jeon E-C 2025 Nanoindentation study on depth-dependent hardness and embrittlement of the ion-irradiated Fe–9Cr alloy *Met. Mater. Int.* **13** 1557–68
- [6] Chai J et al 2025 Microstructure evolution and hardening of helium ion irradiated tungsten *Vacuum* **235** 114153
- [7] Xia L et al 2025 Microstructure evolution and hardening behavior in FCC Ni under ion irradiation: influence of dose rate *Scr. Mater.* **259** 116546
- [8] Hsu T-W, Greczynski G, Boyd R, Kolozsvári S, Polcik P and Odén M 2023 Dense and hard TiWC protective coatings grown with tungsten ion irradiation using WC–HiPIMS/TiC–DCMS co-sputtering technique without external heating *Appl. Surf. Sci.* **618** 156639
- [9] Zhu K, Fan A, Wang J, Chen Z, Chen Y, Liu J, Cheng G, Wu X and Zheng R 2025 Enhancing thermoelectric properties of crystalline silicon through high energy heavy ion irradiation *Appl. Surf. Sci.* **693** 162757
- [10] Fu T, Zhu Y, Pan H, Shi J, Yi T, Xie D, Shen Z, Teng C, Wu Y and Wu L 2024 Irradiation softening in a uranium containing NbTiZrU high entropy alloy induced by Xe ion implantation *Mater. Today Commun.* **42** 111231
- [11] Li D, Chen Y, Zhou C, Shi C, Xu Z, Miao Z, Xi Z and Han J 2024 XPS depth profiling of functional materials: applications of ion beam etching techniques *Mater. Chem. Front.* **8** 715–31
- [12] Dobrovodský J, Vaňa D, Beňo M, Lofaj F and Riedlmajer R 2024 Ion beam analysis including ToF-ERDA of complex composition layers *J. Phys.* **2712** 012024
- [13] Schofield S R et al 2025 Roadmap on atomic-scale semiconductor devices *Nano Futures* **9** 012001
- [14] Maharana B and Chatterjee S 2025 Ion beam engineering of nanostructured materials for superior performance in supercapacitor applications: recent progress and future perspectives *J. Energy Storage* **109** 115039
- [15] Qu W, Guo X and Kang R 2025 Molecular dynamics study of amorphization and defects induced by argon ion implantation into single crystal diamond *Diam. Relat. Mater.* **153** 112063
- [16] Hu P-P et al 2024 Failure mechanisms of AlGaIn/GaN HEMTs irradiated by high-energy heavy ions with and without bias *Nucl. Sci. Tech.* **36** 13
- [17] Fassbender J, Ravelosona D and Samson Y 2004 Tailoring magnetism by light-ion irradiation *J. Phys. D* **37** R179–R196

- [18] Kim H S, Song S, Choi I H, Park S and Lee J S 2024 Surface and bulk characterization of magnetic multilayers formed within a single layer FeRh by hydrogen ion irradiation *J. Alloys Compd.* **1010** 177447
- [19] Zhang Y, Li B, Ren Y, Dai B, Li J, Arslanov T and Wang Y 2025 Evolution of structural and magnetic properties of NiFe/NiO exchange biased bilayer with medium energy C⁺ ion irradiation *J. Alloys Compd.* **1018** 179180
- [20] Cervera S et al 2024 Mastering disorder in a first-order transition by ion irradiation *Phys. Rev. Mater.* **8** 024406
- [21] Mahendra A, Murmu P P, Acharya S K, Islam A, Fiedler H, Gupta P, Granville S and Kennedy J 2023 Shaping perpendicular magnetic anisotropy of Co₂MnGa Heusler alloy using ion irradiation for magnetic sensor applications *Sensors* **23** 4564
- [22] Khanduri H, Dimri M C, Khan S A, Kumar P, Link J, Stern R, Gupta N K and Pant R P 2022 Modifications in ferromagnetic properties of MnAl bilayer thin films induced by swift heavy ion irradiation *J. Mater. Res.* **37** 2468–82
- [23] Gupta R, Lieb K P, Luo Y, Müller G A, Schaaf P and Zhang K 2008 Argon and krypton ion-induced changes in permalloy thin films *Eur. Phys. J. B* **63** 501–6
- [24] Hasegawa T et al 2006 Structural transition from L10 phase to A1 phase in FePt films caused by ion irradiation *J. Appl. Phys.* **99** 053505
- [25] Araki D, Sonobe Y, Takahashi Y K and Homma T 2025 Ultrathin CoPt alloy films with fcc (111) orientation and perpendicular magnetic anisotropy fabricated by electrodeposition *Electrochem. Commun.* **176** 107938
- [26] Yüziak G D 2025 Modifying the magnetic characteristics of ferrimagnetic TbFeCo by adjusting the thickness of the L11-ordered CoPt *J. Alloys Compd.* **1020** 179366
- [27] Walia R, Singh F, Kumar A, Singh V K, Agarwal P C, Chawla V and Chandra R 2024 Swift heavy ions induced transformations in the structural and magnetic properties of Co/Pt multilayer thin films for magnetic storage *Inorg. Chem. Commun.* **170** 113376
- [28] Toyama R, Masuda K, Simalaotao K, Zhou W, Kushwaha V K and Sakuraba Y 2024 Large anomalous Nernst conductivity of L1₀-ordered CoPt in CoPt composition-spread thin films *J. Phys. D* **57** 405001
- [29] Thi Be Lan T, Jane H-J, Ding W-Y, Huang S-Y, Fang L-H, Wu J-C and Sun A A-C 2022 Huge giant-magnetoresistance of Co/Ru/L11-CoPt Multi-layer pseudo-spin valve *J. Alloys Compd.* **938** 168441
- [30] Qiu S, Harumoto T, Nakamura Y and Shi J 2022 Magneto-transport properties of perpendicular magnetization CoPt/VO₂ bilayer films grown on glass substrate *Surf. Coat. Technol.* **436** 128312
- [31] Fan T, Khang N H D, Nakano S and Hai P N 2022 Ultrahigh efficient spin orbit torque magnetization switching in fully sputtered topological insulator and ferromagnet multilayers *Sci. Rep.* **12** 2998
- [32] Dong Y N, Zhao X N, Wang W, Chen Y X, Bai L H, Yan S S and Tian Y F 2022 Room temperature manipulation of exchange bias in magnetic heterojunctions *J. Magn. Mater.* **559** 169546
- [33] Mahendra A, Gupta P, Granville S and Kennedy J 2022 Tailoring of magnetic anisotropy by ion irradiation for magnetic tunnel junction sensors *J. Alloys Compd.* **910** 164902
- [34] Gupta S, Rortais F, Ohshima R, Ando Y, Endo T, Miyata Y and Shiraiishi M 2021 Approaching barrier-free contacts to monolayer MoS₂ employing [Co/Pt] multilayer electrodes *NPG Asia Mater.* **13** 13
- [35] Pedan R et al 2022 Homogenization and short-range chemical ordering of Co-Pt alloys driven by the grain boundary migration mechanism *J. Phys. D* **55** 405004
- [36] Basina G, Alexandrakis V, Panagiotopoulos I, Niarchos D, Devlin E, Gjoka M, Hadjipanayis G C and Tzitzios V 2024 Low-platinum-content exchange-coupled CoPt nanoalloys with enhanced magnetic properties *Nanomaterials* **14** 482
- [37] Li Z W, Jiao J Y, Luo Z, Ma T Y, Qiao L, Wang Y, Wang T and Li F S 2019 Microstructure and magnetic properties of exchange-coupled Co₇₂Pt₂₈/Pt/Co₈₁Ir₁₉ composite media for perpendicular magnetic recording *J. Supercond. Nov. Magn.* **32** 2229–33
- [38] Li W, Harumoto T, Nakamura Y and Shi J 2021 Primitive exchange coupling in CoPt/MnN layered structures: exchange coupling established during deposition *J. Magn. Mater.* **538** 168331
- [39] Liu Y, Xu Y, Fert A, Jaffrès H, Nie T, Eimer S, Zhang X and Zhao W 2024 Efficient orbitronic terahertz emission based on CoPt alloy *Adv. Mater.* **36** 2404174
- [40] Yang L, Li W, Zuo C, Tao Y, Jin F, Li H, Tang R and Dong K 2024 Field-free memristive spin-orbit torque switching in A1 CoPt single layer for image edge detection *Adv. Electron. Mater.* **10** 2300885
- [41] Bonder M J, Telling N D, Grundy P J, Faunce C A, Shen T and Vishnyakov V M 2003 Ion irradiation of Co/Pt multilayer films *J. Appl. Phys.* **93** 7226–8
- [42] Rettner C T, Anders S, Baglin J E E, Thomson T and Terris B D 2002 Characterization of the magnetic modification of Co/Pt multilayer films by He⁺, Ar⁺, and Ga⁺ ion irradiation *Phys. Lett.* **80** 279–81
- [43] Maziewski A et al 2012 Tailoring of magnetism in Pt/Co/Pt ultrathin films by ion irradiation *Phys. Rev. B* **85** 054427
- [44] Som T, Ghosh S, Tripathi J K, Grötzschel R, Mäder M, Ganesan V, Gupta A and Kanjilal D 2008 Tuning magnetic properties of Co/Pt thin films using energetic ions *Nucl. Instrum. Methods Phys. Res. A* **266** 1542–7
- [45] Raj R, Saravanan K, Amirthapandian S and Reddy V R 2024 Control of chiral damping in magnetic trilayers using He⁺ ion irradiation *Appl. Phys. Lett.* **125** 122407
- [46] Pedan R et al 2024 The effect of Ar⁺ and N⁺ ion irradiation on the thermally induced evolution of the structural and magnetic properties of Co/Pt and Pt/Co bilayered stacks *Mater. Chem. Phys.* **327** 129862
- [47] Senichev A, Martin Z O, Wang Y, Matthiessen O M, Lagutchev A, Htoon H, Boltasseva A and Shalaev V M 2024 Quantum emitters in aluminum nitride induced by heavy ion irradiation *APL Quantum* **1** 036103
- [48] Prakash O, Abhijith T, Umopathy G R, Karak S, Singh U B and Ghosh S 2024 Low energy ion irradiation induced Au/Ag multilayer nanostructured substrates for SERS-based molecular sensing *Opt. Mater.* **148** 114814
- [49] Amroussia A, Boehlert C J, Pellemoine F, Grummon D, Mittig W, Bieler T R, Li M and Chen W-Y 2024 Microstructural evolution of ion irradiated commercially pure titanium *J. Nucl. Mater.* **599** 155105
- [50] Yang Y, Zhang Y, Ma X, Li Y, Zhang F, Zhu H, Li D and Wu Z 2025 Defect Engineering in β-Ga₂O₃/4H-SiC heterojunctions via Kr Ion irradiation for enhanced solar-blind photodetector performance *ACS Appl. Mater. Interfaces* **17** 19996–20003
- [51] Was G S 2007 *Fundamentals of Radiation Materials Science* (Springer) (<https://doi.org/10.1007/978-3-540-49472-0>)
- [52] Som T, Ghosh S, Mäder M, Grötzschel R, Roy S, Paramanik D and Gupta A 2007 Temperature-dependent changes in structural and magnetic properties of heavy ion irradiated nanoscale Co/Pt multilayers *New J. Phys.* **9** 164
- [53] Ghosh S, Mäder M, Grötzschel R, Gupta A and Som T 2006 Correlation between phase formation and magnetic properties of heavy ion irradiated CoPt bilayers *Appl. Phys. Lett.* **89** 104104

- [54] Pedan R *et al* 2024 Low-temperature diffusion in thin-film Pt-(Au)-Co heterostructures: a structural and magnetic characterization *Nanotechnology* **35** 195707
- [55] Ziegler J F, Ziegler M D and Biersack J P 2010 SRIM—the stopping and range of ions in matter (2010) *Nucl. Instrum. Methods Phys. Res. A* **268** 1818–23
- [56] Mazalski P *et al* 2021 Ultrathin Co films with Pt and Au covers—magnetic and structural properties driven by Ga⁺ ion irradiation *New J. Phys.* **23** 023015
- [57] Dahmani C E 1985 *Thesis of Louis Pasteur University* (Strasbourg, France)
- [58] Ferrer S, Alvarez J, Lundgren E, Torrelles X, Fajardo P and Boscherini F 1997 Surface x-ray diffraction from Co/Pt(111) ultrathin films and alloys: structure and magnetism *Phys. Rev. B* **56** 9848–57
- [59] Kaye G W C and Laby T H (eds) 1960 *Tables of Physical and Chemical Constants and Some Mathematical Functions* (Longmans Green and Co)
- [60] Benninghoven A, Evans C A, McKeegan K D, Storms H A and Werner H W (eds) 1990 *Secondary Ion Mass Spectrometry* (Wiley)
- [61] Ibusuki T, Kojima S, Kitakami O and Shimada Y 2001 Magnetic anisotropy and behaviors of Fe nanoparticles *IEEE Trans. Magn.* **37** 2223–5
- [62] Kronmüller H 1987 Theory of nucleation fields in inhomogeneous ferromagnets *Phys. Status Solidi b* **144** 385–96
- [63] Netzelmann U 1990 Ferromagnetic resonance of particulate magnetic recording tapes *J. Appl. Phys.* **68** 1800–7
- [64] Kashyap A, Garg K B, Solanki A K, Nautiyal T and Auluck S 1999 Electronic structure, Fermi surface, and curie temperature calculations for the Co-Pt system *Phys. Rev. B* **60** 2262–7
- [65] Toyama R, Kawachi S, Iimura S, Yamaura J-I, Murakami Y, Hosono H and Majima Y 2020 Formation of L10-ordered CoPt during interdiffusion of electron-beam-deposited Pt/Co bilayer thin films on Si/SiO₂ substrates by rapid thermal annealing *Mater. Res. Express* **7** 066101
- [66] Zhang J, Li W, Jones G A and Shen T H 2006 Composition-dependent structural and magnetic properties of Co_{1-x}Pt_x (0.09 ≤ x ≤ 0.86) nanowire arrays *J. Appl. Phys.* **99** 08Q502
- [67] Mandal M, Das B and Mandal K 2009 Synthesis of Co_xPt_{1-x} alloy nanoparticles of different phase by micellar technique and their properties study *J. Colloid Interface Sci.* **335** 40–43
- [68] Wang N, Zhang J, Wang C and Shen T H 2010 A study on phase relations and texture of Co_{1-x}Pt_x (0.09) *Mater. Lett.* **64** 2530–3
- [69] Liu L *et al* 2022 Current-induced self-switching of perpendicular magnetization in CoPt single layer *Nat. Commun.* **13** 3539
- [70] Weller D, Brändle H and Chappert C 1993 Relationship between Kerr effect and perpendicular magnetic anisotropy in Co_{1-x}Pt_x and Co_{1-x}Pd_x alloys *J. Magn. Magn. Mater.* **121** 461–70
- [71] Liou S H, Huang S, Klimek E, Kirby R D and Yao Y D 1999 Enhancement of coercivity in nanometer-size CoPt crystallites *J. Appl. Phys.* **85** 4334–6
- [72] Toyama R, Kawachi S, Yamaura J-I, Murakami Y, Hosono H and Majima Y 2022 Large coercivity of 13 kOe in L10-ordered CoPt on Si/SiO₂ substrates by hydrogen annealing *Jpn. J. Appl. Phys.* **61** 065002
- [73] Zhang Y F, Qin W, Zhang X Y and Wang Y 2004 Nanocomposite Co_{1-x}Pt_x:C films for extremely high-density recording *Phys. Status Solidi a* **201** 3137–41
- [74] Ibusuki T, Sakurai T, Kitakami O and Shimada Y 2001 Synthesis of Co/sub 100-x/Pt/sub x/ alloy fine particles with high coercivity *IEEE Trans. Magn.* **37** 1295–8